J. Fluid Mech. (2009), *vol.* 618, *pp.* 113–134.
doi:10.1017/S0022112008004539 Printed in the United Kingdom

Low-dimensional models of a temporally evolving free shear layer

MINGJUN WEI[1]† AND CLARENCE W. ROWLEY[2]

[1]Department of Mechanical and Aerospace Engineering, New Mexico State University, Las Cruces, NM 88003, USA

[2]Department of Mechanical and Aerospace Engineering, Princeton University, Princeton, NJ 08544, USA

(Received 11 February 2008 and in revised form 24 September 2008)

We develop low-dimensional models for the evolution of a free shear layer in a periodic domain. The goal is to obtain models simple enough to be analysed using standard tools from dynamical systems theory, yet including enough of the physics to model nonlinear saturation and energy transfer between modes (e.g. pairing). In the present paper, two-dimensional direct numerical simulations of a spatially periodic, temporally developing shear layer are performed. Low-dimensional models for the dynamics are obtained using a modified version of proper orthogonal decomposition (POD)/Galerkin projection, in which the basis functions can scale in space as the shear layer spreads. Equations are obtained for the rate of change of the shear-layer thickness. A model with two complex modes can describe certain single-wavenumber features of the system, such as vortex roll-up, nonlinear saturation, and viscous damping. A model with four complex modes can describe interactions between two wavenumbers (vortex pairing) as well. At least two POD modes are required for each wavenumber in space to sufficiently describe the dynamics, though, for each wavenumber, more than 90 % energy is captured by the first POD mode in the scaled space. The comparison of POD modes to stability eigenfunction modes seems to give a plausible explanation. We have also observed a relation between the phase difference of the first and second POD modes of the same wavenumber and the sudden turning point for shear-layer dynamics in both direct numerical simulations and model computations.

1. Introduction

Temporally and spatially evolving shear layers have been studied for over a century (Saffman & Baker 1979; Ho & Huerre 1984; Chomaz 2005), dating back to the early discoveries of Helmholtz and Lord Kelvin, and the more detailed analysis of Lord Rayleigh (Rayleigh 1880), which laid the foundations for the stability analysis we still use today (Schmid & Henningson 2001; Drazin & Reid 2004). Recently, experiments have suggested that high-frequency forcing of shear layers over open cavities may provide a mechanism for suppression of tones in cavities (Stanek *et al.* 2001), and a long-term goal of this work is to study the dynamics of forced shear layers, to understand these effects better and analyse them using techniques for general dynamical systems (Guckenheimer & Holmes 1983; Thomsen 2002). This paper focuses on nonlinear models for the evolution in time of a spatially periodic

† Email address for correspondence: mjwei@nmsu.edu

shear layer, including nonlinear effects such as saturation of disturbances and energy transfer between modes.

The development of these models is motivated by the desire to understand shear flows better, and ultimately to control them. For instance, the free shear layer plays an important role in amplifying disturbances in the flow past a cavity (Tam & Block 1978). A better understanding of these dynamics, and, in particular, nonlinear interactions between frequencies, is essential in order to understand these flows reliably enough to control them (Rowley & Williams 2006).

The technique we use is based on proper orthogonal decomposition (POD) and Galerkin projection, but differs from the standard technique, in that we use basis functions that are able to change their spatial scale as the shear-layer thickness changes. A related technique has been used for travelling solutions in Rowley & Marsden (2000), and self-similar solutions in Rowley *et al.* (2003). In this method, empirical basis functions are computed from numerical data that is first scaled so that it matches best with a preselected 'template'. Forming the reduced-order models in the scaled reference frame is often a considerable advantage, as typically models of much lower dimension are possible once global features such as self-similar spreading have been factored out. Note that POD/Galerkin models of a spatially developing shear layer have been studied by Noack *et al.* (2004), without scaling the modes.

The general philosophy is similar to that used in previous techniques using *shift modes* (Noack *et al.* 2003): we wish to capture the effects of perturbations on the mean flow. However, the specifics of our method are quite different. While shift modes capture the effect on the mean by introducing additional basis functions, we capture these effects by dynamically scaling the coordinates, both of the base flow, and of the basis functions themselves.

Scaling of basis functions is not a new idea: for instance, Noack & Eckelmann (1994) scaled basis functions in the radial direction to model the flow past a cylinder, also using the Galerkin method. However, in this previous work, this scaling was fixed in time, depending on the boundary-layer thickness and Reynolds number. In our work, the basis functions scale dynamically, and a key contribution is equation (3.38), sometimes called a *reconstruction equation*, for how the scaling parameter g changes in time.

In this paper, we consider the complete evolution history of a two-dimensional periodic shear flow, starting with a one-dimensional self-similar solution for shear layer, then instability-induced vortex roll-up, and pairing and, finally, nonlinear saturation and viscous diffusion. This evolution is shown in figure 1. The shear-layer thickness grows throughout the process, and this continuously changing length scale makes it difficult for conventional POD modes to capture the dynamics efficiently.

The main contribution of this paper is a method for scaling the variables so that the dynamics in the scaled frame are as simple as possible. For instance, in this scaled frame, the exact solution for self-similar spreading of a shear layer is simply an equilibrium point. However, the method is not as simple as assuming that the shear layer's spreading rate is the same as that of the self-similar solution: indeed, this would not be appropriate, as the presence of perturbations typically modifies this spreading rate. Instead, we develop an equation for this spreading rate, directly from the Navier–Stokes equations.

The governing equations and other simulation details are given in § 2. Then, we present the scaling technique and low-dimensional modelling in § 3. Finally, in § 4, we compare the model computations with the analytical solution and numerical simulations, and discuss the results.

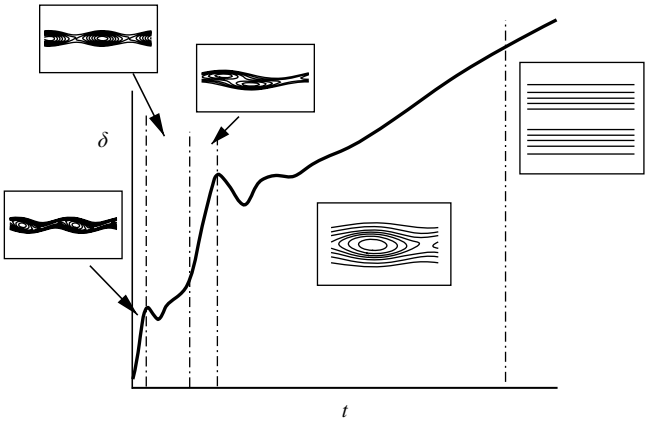

FIGURE 1. Demonstration of typical evolution of periodic shear layers, showing initial growth of the instability, pairing, saturation and viscous diffusion; vorticity contours are shown, but different contour levels are set for better visualization.

2. Governing equations and numerical simulations

The flow considered here is described by non-dimensional Navier–Stokes equations in the form

$$\frac{\partial u}{\partial x}+\frac{\partial v}{\partial y}=0, \tag{2.1a}$$

$$\frac{\partial u}{\partial t}+u\frac{\partial u}{\partial x}+v\frac{\partial u}{\partial y}=-\frac{\partial p}{\partial x}+\frac{1}{Re}\left(\frac{\partial^2 u}{\partial x^2}+\frac{\partial^2 u}{\partial y^2}\right), \tag{2.1b}$$

$$\frac{\partial v}{\partial t}+u\frac{\partial v}{\partial x}+v\frac{\partial v}{\partial y}=-\frac{\partial p}{\partial y}+\frac{1}{Re}\left(\frac{\partial^2 v}{\partial x^2}+\frac{\partial^2 v}{\partial y^2}\right), \tag{2.1c}$$

where the characteristic length is the initial vorticity thickness $\delta_{\omega 0}$ at $t=0$, and the characteristic velocity is $\Delta U=U_2-U_1$ with U_1 and U_2 being the velocities at $-\infty$ and $+\infty$. We define vorticity thickness for shear layers as $\delta_\omega=(U_2-U_1)/|\mathrm{d}u/\mathrm{d}y|_{\max}$ (Brown & Roshko 1974). Accordingly, the pressure is scaled by $\rho\Delta U^2$ and Reynolds number is defined by $Re=\rho\Delta U\delta_{\omega 0}/\mu$. For the rest of the paper, all variables are normalized by the same characteristic values unless otherwise specified. Though incompressible flow is assumed here and later in low-dimensional modelling, the simulations solve the fully compressible Navier–Stokes equations at low Mach number ($M_c=(U_2+U_1)/2a_\infty=0.2$), using a code that has been extensively validated before for a spatially developing shear layer by Wei & Freund (2006). The velocity divergence induced by weak compressibility has been checked to be negligible, and thus treating the current simulation data as 'incompressible' is justified. This approximation is also assured by the comparison between the results from numerical simulation, analytical solution (one-dimensional viscous diffusion case only), and the model presented later in this paper.

As shown in figure 2, a two-dimensional free shear flow, periodic along the streamwise (x) direction with Reynolds number $Re=200$, is simulated in a rectangular region of $0<x<5\pi$ and $-50<y<50$ with 128×800 mesh points along the x- and y-directions. The domain length was chosen to be about twice the wavelength of the most unstable mode for the initial shear-layer profile, and the mesh was stretched in y to increase the resolution in the shear layer. The computational domain includes

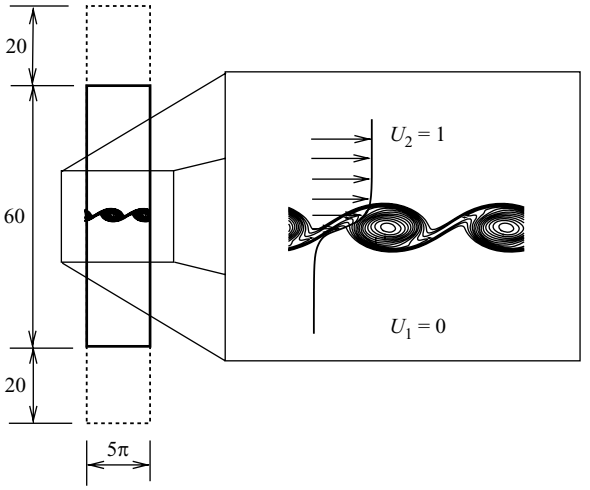

FIGURE 2. Schematic of the two-dimensional free-shear-layer simulation.

an absorbing buffer zone (Freund 1997) at the top and bottom ($30 < |y| < 50$), which mimics the radiation boundary conditions, along with a one-dimensional characteristic boundary condition at the outside boundaries. A periodic boundary condition is applied naturally along the x-direction. A spectral method was used for the x-direction derivatives, the fourth-order dispersion-relation-preserving scheme of Tam & Webb (1993) was used for derivatives along the y-direction, with a fourth-order Runge–Kutta algorithm for time advancement.

2.1. *Exact solution*

Using classical similarity solution techniques (Schlichting & Gersten 2000), we can show there exists an unstable self-similar solution

$$u_s(\eta) = U_1 + \frac{U_2 - U_1}{2}\mathrm{erfc}(-\eta), \qquad v_s(\eta) = 0, \tag{2.2}$$

where the similarity variable η is given by

$$\eta = y\left(\frac{Re}{4(t - t_0)}\right)^{1/2}. \tag{2.3}$$

Here, we use this exact solution for three purposes: as a base flow, about which to expand the solution in terms of modes, as in (3.8); as a *template function*, to be defined in the next section, as used in (3.5); and in order to validate our numerical simulations and low-order model formulation. We typically take the singularity time t_0 to be $-Re/4$, so that $\eta = y$ at $t = 0$. In all simulations, we choose $U_1 = 0$ and $U_2 = 1$. Then the initial velocity field for the simulation is simply

$$u_0(y) = \tfrac{1}{2}\mathrm{erfc}(-y), \qquad v_0 = 0. \tag{2.4}$$

Although we use this self-similar solution as a base flow, note that the derivation of all model equations below, including the evolution of the scaling variable, has *no underlying assumption of self-similarity*. This preserves the generality of the current modelling effort, and allows us to study solutions that are not precisely self-similar, but rather are perturbations of self-similar solutions.

3. Low-dimensional models

3.1. *Scaling and mode decomposition*

A common approach to low-dimensional modelling is to project the governing equations onto a fixed set of basis functions, which are often determined by POD of a set of data. Here, since the shear-layer thickness is spreading in time, we consider basis functions that scale in the y-direction. In particular, denoting the vector of flow velocity by $\boldsymbol{q} = (u, v)$, we introduce a scaled variable $\tilde{\boldsymbol{q}}$, which satisfies

$$\boldsymbol{q}(x, y, t) = \mathbf{G}(g)\tilde{\boldsymbol{q}}(x, g(t)y, t), \tag{3.1}$$

where $g(t) > 0$ is a scaling factor, and a coefficient matrix

$$\mathbf{G}(g) = \begin{bmatrix} 1 & 0 \\ 0 & 1/g \end{bmatrix} \tag{3.2}$$

is introduced so that, for any $g(t) > 0$,

$$\mathrm{div}\boldsymbol{q} = 0 \iff \mathrm{div}\tilde{\boldsymbol{q}} = 0. \tag{3.3}$$

The pressure is scaled similarly by

$$p(x, y, t) = \tilde{p}(x, g(t)y, t).$$

Later, it is shown that once boundary conditions are imposed, the pressure terms disappear as long as a particular definition of the inner product is used. This avoids the need to model the pressure term explicitly as in Noack *et al.* (2005). Therefore, we focus our discussion below on the flow velocity vector $\tilde{\boldsymbol{q}}$.

Writing $\tilde{\boldsymbol{q}}$ in terms of its components $(\tilde{u}, \tilde{v})$, the scaling relation becomes

$$u(x, y, t) = \tilde{u}(x, g(t)y, t), \tag{3.4a}$$

$$v(x, y, t) = \frac{1}{g}\tilde{v}(x, g(t)y, t). \tag{3.4b}$$

The choice of the scaling factor $g(t)$ is arbitrary, but following the approach in Rowley *et al.* (2003), here we choose it so that the scaled solution $\tilde{\boldsymbol{q}}(x, y, t)$ lines up best with a pre-selected template function. The exact solution is a natural choice for a template function, so we take the template function to be $\boldsymbol{q}_0 = (u_0, v_0)$ as well. Since only the u-component of the template velocity is non-zero, the scaling factor $g(t)$ in this paper is defined as

$$g(t) = \arg\min_g \left\| u\left(x, \frac{y}{g}, t\right) - u_0(y) \right\|^2, \tag{3.5}$$

where the L^2 norm is defined by an integration over the spatial domain Ω (over all y and one period along x):

$$\|\cdot\|^2 = \int_\Omega (\cdot)^2 \,\mathrm{d}x\,\mathrm{d}y. \tag{3.6}$$

A new thickness δ_g can be defined by $g(t)$ as

$$\delta_g = 1/g(t). \tag{3.7}$$

It is not surprising that the thickness δ_g is very close to δ_ω in our flow, and therefore, all qualitative statements we make about δ_g and δ_ω are interchangeable.

We can expand the scaled velocity $\tilde{\boldsymbol{q}}$ in terms of basis functions $\boldsymbol{\Phi}_j$, using the exact solution as a base flow, as

$$\tilde{\boldsymbol{q}}(x, y, t) = \boldsymbol{q}_0(y) + \sum_{j=1}^{\infty} a_j(t)\boldsymbol{\Phi}_j(x, y), \tag{3.8}$$

where $\boldsymbol{\Phi}_j$ are basis functions and a_j are corresponding time coefficients. We note that in practice, $\boldsymbol{q}_0$ is very close (almost identical) to the mean (in x and t) of the scaled data from the simulations.

Because of the translation invariance in the x-direction, Fourier modes are an appropriate choice along the x-direction for our problem. Along the y-direction, we first scale all data snapshots as in (3.1) so that each snapshot most closely matches the template $u_0(y)$, as described in (3.5). We then compute the POD modes of each wavenumber from the scaled data set. The expansion (3.8) becomes

$$\tilde{\boldsymbol{q}}(x, y, t) = \tilde{\boldsymbol{q}}_0(y) + \sum_{k=-\infty}^{+\infty} \sum_{n=0}^{\infty} a_{k,n}(t)\boldsymbol{\Phi}_{k,n}(x, y), \tag{3.9}$$

with basis functions

$$\boldsymbol{\Phi}_{k,n}(x, y) = \mathrm{e}^{2\pi \mathrm{i} k x/L}\phi_{k,n}(y). \tag{3.10}$$

Here, k is the wavenumber with L being the total domain length in the x-direction, and $\phi_{k,n} = (\hat{u}_{k,n}, \hat{v}_{k,n})$ is the nth POD mode for wavenumber k. The vector inner product used in the POD calculation is simply

$$\langle \tilde{\boldsymbol{a}}, \tilde{\boldsymbol{b}} \rangle = \int_{\Omega} (\tilde{a}_1\tilde{b}_1 + \tilde{a}_2\tilde{b}_2)\,\mathrm{d}x\,\mathrm{d}y, \tag{3.11}$$

where $\tilde{\cdot}$ indicates that the quantity is in the scaled space, and the x integration is actually absorbed during the computation after each individual Fourier mode is substituted in. The energy of each POD mode (k, n) is quantified by

$$\lambda_{k,n} = \overline{|\langle \tilde{\boldsymbol{q}} - \tilde{\boldsymbol{q}}_0, \Phi_{k,n} \rangle|^2} = \overline{|a_{k,n}|^2}, \tag{3.12}$$

where $\bar{\cdot}$ denotes a time average. We emphasize that the inner product used here to compute POD modes is different from the one used later in Galerkin projection, defined in (3.27). As a result, the orthogonality of POD modes cannot be assumed when the flow equations are projected to these bases.

3.2. *Projection of flow equations*

From a more general point of view, we regard the equations of motion as a dynamical system evolving on a function space H, consisting of the flow variables at all points (x, y) in our spatial domain. Thus, $\boldsymbol{q}(t) \in H$ is a snapshot of the entire flow at time t, and the governing equations of motion may be written

$$\frac{\partial \boldsymbol{q}(t)}{\partial t} = f(\boldsymbol{q}(t)), \tag{3.13}$$

where f is a differential operator on H (e.g. the Euler or Navier–Stokes equations). If we introduce the scaling operator $S_g : H \to H$, defined by

$$S_g[\boldsymbol{q}](x, y) = \boldsymbol{G}(g)\boldsymbol{q}(x, gy), \qquad \forall g \in \mathbb{R}^+, \tag{3.14}$$

then the scaling (3.1) becomes $\boldsymbol{q}(t) = S_g[\tilde{\boldsymbol{q}}(t)]$, and the governing equations may be written

$$\frac{\partial}{\partial t} S_{g(t)}[\tilde{\boldsymbol{q}}(t)] = f(S_g[\tilde{\boldsymbol{q}}(t)]). \tag{3.15}$$

Since

$$\begin{aligned}
\frac{\partial}{\partial t} S_{g(t)}[\tilde{\boldsymbol{q}}(t)](x, y) &= \frac{\partial}{\partial t}\mathbf{G}(g)\tilde{\boldsymbol{q}}(x, g(t)y, t) \\
&= \left(\frac{\partial}{\partial t}\mathbf{G}(g)\right)\tilde{\boldsymbol{q}}(x, g(t)y, t) + \mathbf{G}(g)\frac{\partial}{\partial t}\tilde{\boldsymbol{q}}(x, g(t)y, t) \\
&= \dot{\mathbf{G}}(g, \dot{g})\tilde{\boldsymbol{q}}(x, g(t)y, t) + \mathbf{G}(g)\frac{\partial \tilde{\boldsymbol{q}}}{\partial t}(x, gy, t) + \mathbf{G}(g)\dot{g}y\frac{\partial \tilde{\boldsymbol{q}}}{\partial y}(x, gy, t) \\
&= \dot{\mathbf{G}}(g, \dot{g})\tilde{\boldsymbol{q}}(x, g(t)y, t) + S_g\left[\frac{\partial \tilde{\boldsymbol{q}}}{\partial t}\right](x, y) + \frac{\dot{g}}{g} S_g\left[y\frac{\partial \tilde{\boldsymbol{q}}}{\partial y}\right](x, y),
\end{aligned} \tag{3.16}$$

where

$$\dot{\mathbf{G}}(g, \dot{g}) = \begin{bmatrix} 0 & 0 \\ 0 & -\dot{g}/g^2 \end{bmatrix}, \tag{3.17}$$

the equations of motion become

$$S_g\left[\frac{\partial \tilde{\boldsymbol{q}}}{\partial t}\right] = f(S_g[\tilde{\boldsymbol{q}}]) - \frac{\dot{g}}{g} S_g\left[y\frac{\partial \tilde{\boldsymbol{q}}}{\partial y}\right] - \dot{\mathbf{G}}(g, \dot{g})\tilde{\boldsymbol{q}}(x, gy, t). \tag{3.18}$$

If we define $f_g(\tilde{\boldsymbol{q}}) = S_{1/g} f(S_g[\tilde{\boldsymbol{q}}])$, then these may be written

$$\frac{\partial \tilde{\boldsymbol{q}}}{\partial t} = f_g(\tilde{\boldsymbol{q}}) - \frac{\dot{g}}{g} y\frac{\partial \tilde{\boldsymbol{q}}}{\partial y} - \mathbf{G}(1/g)\dot{\mathbf{G}}(g, \dot{g})\tilde{\boldsymbol{q}}(x, y, t). \tag{3.19}$$

Thus, the equations for the evolution of the scaled variable $\tilde{\boldsymbol{q}}$ are similar to the original dynamics (3.13), with f replaced by f_g, and with two additional terms related to the rate of change of the scaling factor $g(t)$.

Applying the results to our flow equations in (2.1*a*), the function $f(\boldsymbol{q})$ for the Navier–Stokes equations is

$$f(\boldsymbol{q}) = \boldsymbol{C}(\boldsymbol{q}, \boldsymbol{q}) + \boldsymbol{P} + \frac{1}{Re}\boldsymbol{V}(\boldsymbol{q}), \tag{3.20}$$

where

$$\begin{aligned}
\boldsymbol{C}(\boldsymbol{q}_1, \boldsymbol{q}_2) &= \begin{pmatrix} -u_1\dfrac{\partial u_2}{\partial x} - v_1\dfrac{\partial u_2}{\partial y} \\ -u_1\dfrac{\partial v_2}{\partial x} - v_1\dfrac{\partial v_2}{\partial y} \end{pmatrix}, \\
\boldsymbol{P} = \begin{pmatrix} -\dfrac{\partial p}{\partial x} \\ -\dfrac{\partial p}{\partial y} \end{pmatrix}, \quad \boldsymbol{V} &= \begin{pmatrix} \dfrac{\partial^2 u}{\partial x^2} + \dfrac{\partial^2 u}{\partial y^2} \\ \dfrac{\partial^2 v}{\partial x^2} + \dfrac{\partial^2 v}{\partial y^2} \end{pmatrix}.
\end{aligned} \tag{3.21}$$

Following the derivation above, it is straightforward to obtain $f_g(\tilde{\boldsymbol{q}})$ as

$$f_g(\tilde{\boldsymbol{q}}) = \boldsymbol{C}_g(\tilde{\boldsymbol{q}}, \tilde{\boldsymbol{q}}) + \boldsymbol{P}_g + \frac{1}{Re}\boldsymbol{V}_g(\tilde{\boldsymbol{q}}), \tag{3.22}$$

where

$$\boldsymbol{C}_g(\tilde{\boldsymbol{q}}, \tilde{\boldsymbol{q}}) = \begin{pmatrix} -\tilde{u}\dfrac{\partial \tilde{u}}{\partial x} - \tilde{v}\dfrac{\partial \tilde{u}}{\partial y} \\ -\tilde{u}\dfrac{\partial \tilde{v}}{\partial x} - \tilde{v}\dfrac{\partial \tilde{v}}{\partial y} \end{pmatrix}, \quad \boldsymbol{P}_g = \begin{pmatrix} -\dfrac{\partial \tilde{p}}{\partial x} \\ -g^2\dfrac{\partial \tilde{p}}{\partial y} \end{pmatrix}, \quad \boldsymbol{V}_g(\tilde{\boldsymbol{q}}) = \begin{pmatrix} \dfrac{\partial^2 \tilde{u}}{\partial x^2} + g^2\dfrac{\partial^2 \tilde{u}}{\partial y^2} \\ \dfrac{\partial^2 \tilde{v}}{\partial x^2} + g^2\dfrac{\partial^2 \tilde{v}}{\partial y^2} \end{pmatrix}. \tag{3.23}$$

At the same time, with the scaling $(u, v) \to (\tilde{u}, \tilde{v})$ defined in (3.1), the scaled velocity field remains divergence free:

$$\frac{\partial \tilde{u}}{\partial x} + \frac{\partial \tilde{v}}{\partial y} = 0. \tag{3.24}$$

Since the basis functions are linear combinations of flow snapshots, each basis function for the scaled space is also divergence free:

$$\operatorname{div}\boldsymbol{\Phi}_{k,n} = 0, \tag{3.25}$$

which indicates that the continuity equation is automatically satisfied in the scaled space by the decomposition (3.9). The continuity equation is also used to remove pressure terms as shown later.

Initially, to simplify the discussion, we retain only wavenumbers $k = \pm 1$, and the first two POD modes $n = 1$ and $n = 2$ for each wavenumber in the expansion of $\tilde{\boldsymbol{q}}$ in (3.9). The summation is then an approximation of the original $\tilde{\boldsymbol{q}}$. We will abuse notation and retain the notation $\tilde{\boldsymbol{q}}$ for the finite sum in (3.9). Since $\tilde{\boldsymbol{q}}$ must be real, we have the additional constraint that

$$a_{1,1}\boldsymbol{\Phi}_{1,1} + a_{1,2}\boldsymbol{\Phi}_{1,2} = a^*_{-1,1}\boldsymbol{\Phi}^*_{-1,1} + a^*_{-1,2}\boldsymbol{\Phi}^*_{-1,2}, \tag{3.26}$$

which permits further simplification of the equations that follow.

To obtain the equations for time coefficients $a_{1,1}(t)$ and $a_{1,2}(t)$, we project the governing equation (3.19) onto modes $\boldsymbol{\Phi}_{1,1}$ and $\boldsymbol{\Phi}_{1,2}$. The inner product for the projection in the scaled space is g-dependent and defined by

$$\langle \tilde{\boldsymbol{a}}, \tilde{\boldsymbol{b}} \rangle_g = \int_\Omega \left(\frac{1}{g} a_1 b_1 + \frac{1}{g^3} a_2 b_2 \right) \mathrm{d}x\, \mathrm{d}y, \tag{3.27}$$

for which the following identity holds:

$$\langle \boldsymbol{q}_1, \boldsymbol{q}_2 \rangle = \langle \tilde{\boldsymbol{q}}_1, \tilde{\boldsymbol{q}}_2 \rangle_g . \tag{3.28}$$

Note that this definition of the inner product causes the pressure terms to vanish: we have

$$\langle \boldsymbol{P}_g, \boldsymbol{\Phi}_{k,n} \rangle_g = 0, \tag{3.29}$$

since $\boldsymbol{\Phi}_{k,n}$ is divergence-free and either vanishes or is periodic at the boundaries, in a way similar to the discussion by Holmes, Lumley & Berkooz (1996). For other problems with more general boundary conditions, modelling the pressure terms explicitly may be necessary, as described by Noack *et al.* (2005).

Therefore, the projected flow equations on basis function $\boldsymbol{\Phi}_{k,n}$ are

$$\left\langle \frac{\partial \tilde{\boldsymbol{q}}}{\partial t}, \boldsymbol{\Phi}_{k,n} \right\rangle_g = \langle \boldsymbol{C}_g(\tilde{\boldsymbol{q}}, \tilde{\boldsymbol{q}}), \boldsymbol{\Phi}_{k,n} \rangle_g + \frac{1}{Re} \langle \boldsymbol{V}_g(\tilde{\boldsymbol{q}}), \boldsymbol{\Phi}_{k,n} \rangle_g + \left\langle -\frac{\dot{g}}{g} y \frac{\partial \tilde{\boldsymbol{q}}}{\partial y} - \mathbf{G}(1/g)\dot{\mathbf{G}}(g, \dot{g})\tilde{\boldsymbol{q}}(x, y, t), \boldsymbol{\Phi}_{k,n} \right\rangle_g . \tag{3.30}$$

With the values substituted for mode $\boldsymbol{\Phi}_{1,1}$ and $\boldsymbol{\Phi}_{1,2}$, eventually, we obtain the evolution equations for coefficient vector $\boldsymbol{a} = (a_{1,1}\ \ a_{1,2})^T$:

$$\boldsymbol{A}\dot{\boldsymbol{a}} = \left(\boldsymbol{B} + \frac{1}{Re}\boldsymbol{D} + \frac{\dot{g}}{g}\boldsymbol{E}\right)\boldsymbol{a}, \tag{3.31}$$

where matrices $\boldsymbol{A}$, $\boldsymbol{B}$, $\boldsymbol{D}$, and $\boldsymbol{E}$ are defined by

$$\boldsymbol{A} = \begin{bmatrix} g^2 n_{11g} + n_{11} & g^2 n_{12g} + n_{12} \\ g^2 n_{21g} + n_{21} & g^2 n_{22g} + n_{22} \end{bmatrix}, \quad \boldsymbol{B} = \begin{bmatrix} g^2 c_{11g} + c_{11} & g^2 c_{12g} + c_{12} \\ g^2 c_{21g} + c_{21} & g^2 c_{22g} + c_{22} \end{bmatrix}, \tag{3.32a, b}$$

$$\boldsymbol{D} = \begin{bmatrix} -(2\pi/L)^2(g^2 n_{11g} + n_{11}) + (g^2 d_{11g} + d_{11})g^2 \\ -(2\pi/L)^2(g^2 n_{12g} + n_{12}) + (g^2 d_{12g} + d_{12})g^2 \\ -(2\pi/L)^2(g^2 n_{21g} + n_{21}) + (g^2 d_{21g} + d_{21})g^2 \\ -(2\pi/L)^2(g^2 n_{22g} + n_{22}) + (g^2 d_{22g} + d_{22})g^2 \end{bmatrix}, \tag{3.32c}$$

$$\boldsymbol{E} = \begin{bmatrix} g^2 e_{11g} + e_{11} & g^2 e_{12g} + e_{12} \\ g^2 e_{21g} + e_{21} & g^2 e_{22g} + e_{22} \end{bmatrix}. \tag{3.32d}$$

Note that the quadratic term due to $\boldsymbol{C}_g$ does not appear, because only wavenumbers ± 1 are retained. All coefficients above are constants (depending only on the basis functions), and defined in Appendix A.

3.3. *Equations of motion for the thickness*

In the scaled space, the flow equations alone are not enough to specify the evolution $\tilde{\boldsymbol{q}}(t)$, however, as we also need to specify the scaling $g(t)$.

Following (3.5), the condition that $\tilde{u}$ be scaled so that it most closely matches u_0 may be written

$$\left.\frac{\mathrm{d}}{\mathrm{d}s}\right|_{s=0} \|\tilde{u}(x, y, t) - u_0(h(s)y)\|^2 = 0,$$

where $h(s)$ is any curve in $\mathbb{R}^+$ with $h(0) = 1$, and $\|\cdot\|^2$ is the same norm as before on the space of functions of (x, y): that is, $h = 1$ is a local minimum of the error norm above. This expression becomes

$$-2\left\langle \left.\frac{\mathrm{d}}{\mathrm{d}s}\right|_{s=0} u_0(h(s)y), \tilde{u}(x, y, t) - u_0(y) \right\rangle = 0,$$

which becomes

$$\left\langle y\frac{\partial u_0}{\partial y}, \tilde{u} - u_0 \right\rangle = 0. \tag{3.33}$$

Geometrically, this result means that the set of all such functions $\tilde{u}$ that are scaled so that they most closely match the template u_0 is an affine space through u_0 and orthogonal to $y\partial_y u_0$. Since only scalar values are involved, the different definitions for vector inner products before have no impact here. For clarity, however, the scalar inner product is defined in the same domain by

$$\langle a, b \rangle = \int_\Omega (ab)\,\mathrm{d}x\,\mathrm{d}y. \tag{3.34}$$

Differentiating the constraint (3.33), we have

$$\left\langle y\frac{\partial u_0}{\partial y}, \frac{\partial \tilde{u}}{\partial t}\right\rangle = 0. \tag{3.35}$$

If (3.19) is written separately in $\tilde{u}$ and $\tilde{v}$ as

$$\frac{\partial \tilde{u}}{\partial t} = f_g^1(\tilde{u}) - \frac{\dot{g}}{g} y\frac{\partial \tilde{u}}{\partial y}, \tag{3.36a}$$

$$\frac{\partial \tilde{v}}{\partial t} = f_g^2(\tilde{v}) - \frac{\dot{g}}{g} y\frac{\partial \tilde{v}}{\partial y} + \frac{\dot{g}}{g}\tilde{v}, \tag{3.36b}$$

we have

$$\left\langle y\frac{\partial u_0}{\partial y}, f_g^1(\tilde{u}) - \frac{\dot{g}}{g} y\frac{\partial \tilde{u}}{\partial y}\right\rangle = 0, \tag{3.37}$$

which becomes

$$\frac{\dot{g}}{g} = \frac{\langle f_g^1(\tilde{u}), y\partial_y u_0\rangle}{\langle y\partial_y \tilde{u}, y\partial_y u_0\rangle}. \tag{3.38}$$

With f_g^1 defined from (3.22) and the finite expansion (two modes only) of (3.9) being substituted, ultimately, the system is closed by the evolution equation of scaling variable g:

$$\dot{g} = \frac{c_{01}}{n_0} a_{1,1}a_{1,1}^* g + \frac{c_{02}}{n_0} a_{1,2}a_{1,2}^* g + \frac{c_{03}}{n_0} a_{1,1}a_{1,2}^* g + \frac{c_{04}}{n_0} a_{1,2}a_{1,1}^* g + \frac{1}{Re}\frac{d_0}{n_0} g^3, \tag{3.39}$$

where the constant coefficients are defined in Appendix A.

If we choose two more modes $n = 1$ and 2 for wavenumber $k = 2$, the same derivation can give the equations of g, $a_{1,1}$, $a_{1,2}$, $a_{2,1}$ and $a_{2,2}$ to describe more complex physics. The resulting equations are lengthy, however, and are given in Appendix B.

4. Results and discussions

In order to validate our numerical scheme as well as our scaling procedure, we first compare our simulations against the exact self-similar solution (2.2). Then, two more complex cases are studied, starting with small initial perturbations, chosen to be eigenfunctions corresponding to the most unstable modes for wavenumbers $k = 1$ and 2, respectively. The case started with the most unstable $k = 1$ mode is dominated by a single $k = 1$ wavenumber, as we expect. The case with the $k = 2$ mode as the initial perturbation is dominated by the $k = 2$ mode initially, and then pairing occurs, once the $k = 1$ mode becomes more unstable as the shear layer spreads. In this case, both $k = 1$ and $k = 2$ modes are required in order to model this behaviour.

4.1. *One-dimensional laminar diffusion solution*

If the flow starts with the velocity profile in (2.4) and no perturbation is added throughout the process, the dynamics should follow the self-similar solution

$$u(y, t) = u_0(\eta(y, t)), \qquad v = 0, \tag{4.1}$$

with $\eta(y, t)$ given by (2.3) with $t_0 = -Re/4$. We will show that the method of § 3 retrieves this solution analytically.

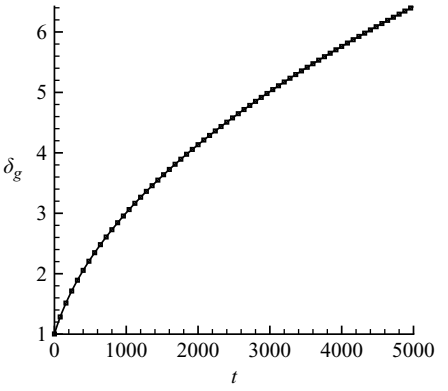

FIGURE 3. Thickness δ_g for self-similar solution: ——, DNS data; ■, model (4.4).

The coefficients $a_{k,n}$ in (3.31) are initially zero, therefore remain zero for all time, and (3.39) simplifies to

$$\dot{g} = \frac{1}{Re}\frac{d_0}{n_0}g^3. \tag{4.2}$$

Substituting u_0 from (2.4) into the equations for n_0 and d_0 in Appendix A, we have

$$n_0 = \frac{1}{\pi}\int y^2 \exp(-2y^2)\,\mathrm{d}y, \tag{4.3a}$$

$$d_0 = -\frac{2}{\pi}\int y^2 \exp(-2y^2)\,\mathrm{d}y, \tag{4.3b}$$

and (4.2) therefore reduces to

$$\dot{g} = -\frac{2}{Re}g^3. \tag{4.4}$$

Solving (4.4) with initial condition $g(0) = 1$ gives

$$g(t) = \left(\frac{Re}{4t + Re}\right)^{1/2}. \tag{4.5}$$

With $t_0 = -Re/4$ in (2.3), we have $\eta(t) = yg(t)$, and thus the solution

$$u(x, y, t) = u_0(g(t)y), \qquad v = 0, \tag{4.6}$$

given by (3.4*b*) and (3.9), matches the analytical solution in (4.1).

Figure 3 shows a comparison of the thickness δ_g, defined in (3.7), comparing the exact solution $g(t)$ from (4.5) to the value computed from the direct numerical simulation. The two are visually identical, affirming that the weakly compressible simulation accurately models the incompressible flow.

4.2. *Shear-layer vortex transient*

Next, we consider the flow with an initial perturbation containing only the $k = 1$ wavenumber. Here, the most unstable eigenfunction for $k = 1$ (figure 4) was introduced with a very small amplitude, $0.02\Delta U$, to initiate the instability. We have confirmed that both simulation and model results are not sensitive to this initial amplitude. In figure 4, only the $\hat{v}$ component is shown (as is typical in shear-layer instability studies (Schmid & Henningson 2001)), and $\hat{u}$ can be obtained from the continuity equation.

(k, n)	λ	Energy (%)
(1, 1)	130.3	91.0
(1, 2)	6.8	4.8
(2, 1)	4.5	3.1
All $k=0$		0.4

TABLE 1. Energy contained in different modes for the flow with $k=1$ initial perturbation.

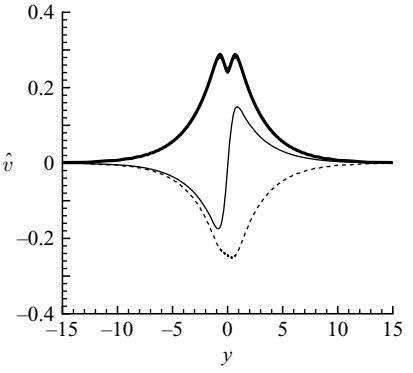

FIGURE 4. $\hat{v}$ of the most unstable eigenfunction for $k=1$. The thin solid line represents the real value, the thin dashed line represents the imaginary value, and the thick solid line represents the absolute value.

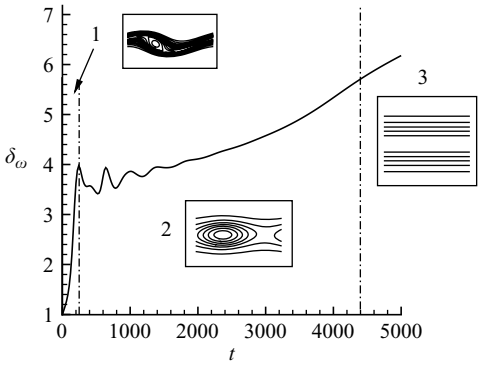

FIGURE 5. Vorticity thickness δ_ω for the flow with $k=1$ initial perturbation: three developing stages are marked, corresponding to 1, growth of the instability; 2, nonlinear saturation; and 3, pure viscous dissipation.

The time evolution of the shear-layer thickness is shown in figure 5. From this figure, we can identify three developing stages: 1, vortices with wavenumber $k=1$ roll up and cause rapid growth of the shear-layer thickness; 2, the flow becomes stable as the shear layer thickens, vortices start to decrease in strength, and viscous dissipation starts to play the main role in the shear-layer thickness spreading; 3, all perturbations have decayed, and the profile simply spreads by viscous dissipation.

For this case, table 1 shows that the first POD mode ($n=1$) of $k=1$ contains most of the energy (91.0 %), the second POD mode ($n=2$) of $k=1$ and the first POD mode ($n=1$) of $k=2$ contain a small amount of energy, and the remaining modes

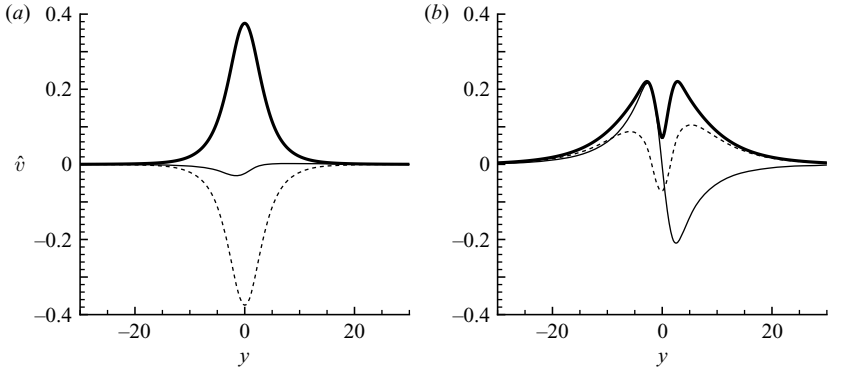

FIGURE 6. $\hat{v}$ for POD mode (*a*) $(k, n) = (1, 1)$ and (*b*) $(k, n) = (1, 2)$. The thin solid line represents the real value, the thin dashed line represents the imaginary value, and the thick solid line represents the absolute value.

contain very little energy. Note that all $k = 0$ modes together comprise only 0.4 % of the total energy, which indicates that the scaling has efficiently separated out the spreading of the mean flow.

Below, we will refer to the mode with, e.g. $k = 1$ and $n = 2$ as the (1, 2) mode. Notice from table 1 that the (1, 2) and (2, 1) modes contain a small amount of energy at about the same level. However, in forming reduced-order models, we notice that mode (1, 2) seems to be more dynamically important in the sense of capturing the system evolution features with low-order models. Later, we will show that keeping only (1, 1) and (1, 2) modes can produce reasonably accurate models, whereas the same size model with (1, 1) and (2, 1) modes does not perform as well. These most dynamically important modes, (1, 1) and (1, 2) are shown in figure 6 (again, only $\hat{v}$ is shown). Note that modes $n = 1$ and $n = 2$ have different symmetries (as evident from their real parts), and their absolute values have different shapes near $y = 0$. By comparing the modes to eigenfunctions of the most unstable mode for $k = 1$ (figure 4), we may argue that the dip at the centre created by mode $n = 2$ helps to form a shape similar to the unstable eigenfunction and therefore couples to the natural instability (vortex roll-up). This hypothesis can also explain why retaining the $n = 2$ mode in our Galerkin projection is important, even though it contains only a small fraction of the energy. Similar behaviour will be seen in § 4.3 for the case with two dominant frequencies.

The time coefficients $a_{1,1}(t)$ and $a_{1,2}(t)$ of modes (1, 1) and (1, 2), respectively, are shown in figure 7(*a*) (for all time coefficients a, only the real part is shown). On comparing to the time evolution of the thickness δ_g, we can clearly identify the three developing stages described before, corresponding to growth, saturation, and purely viscous dissipation once the perturbations have decayed. Simulations of the two-mode model, retaining only $(k, n) = (1, 1)$ and (1, 2) modes, are shown in figure 7(*b*), for the same initial condition as in figure 7(*a*). The model successfully captures the dynamic features in all three developing stages. The model solution grows more in stage 1, and is more violent but stabilized at about the same time in stage 2. The same viscous diffusion appears in stage 3 as we can expect from the comparison to the previous one-dimensional diffusion solution.

Figure 7(*a*) also illustrates a relation between the phase difference between the coefficients $a_{1,1}$ and $a_{1,2}$, and the thickness growth: as the perturbation grows, the

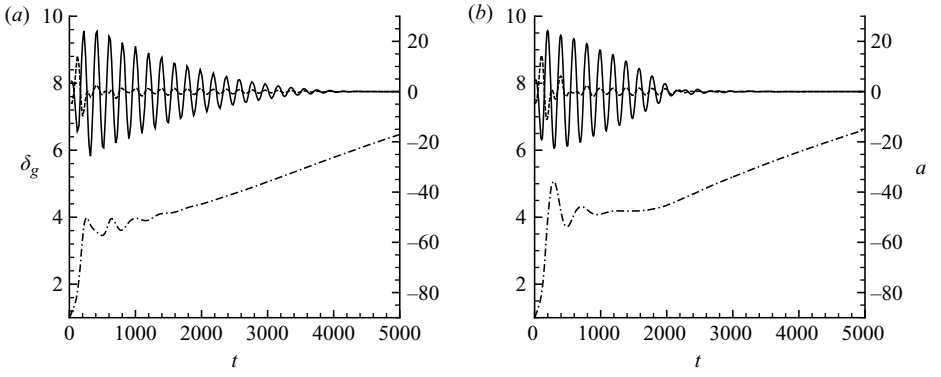

FIGURE 7. Comparison of dynamic behaviour of the flow with $k=1$ initial perturbation: (a) the projection of the full simulation; (b) the solution of the two-mode model. ——, time coefficients $a_{1,1}(t)$; — — —, time coefficients $a_{1,2}(t)$; — · —·, shear-layer thickness δ_g.

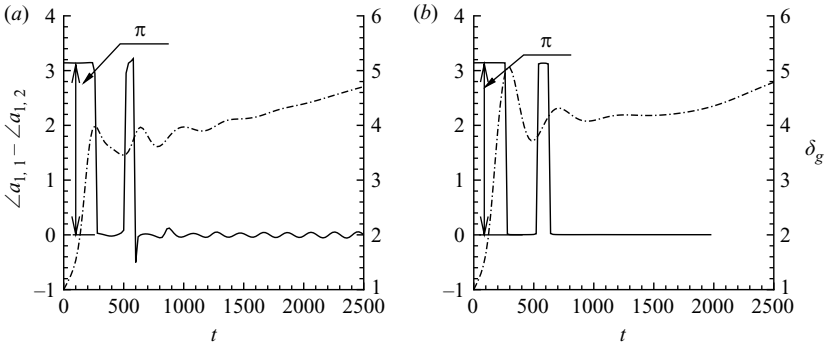

FIGURE 8. Relation between the shear-layer thickness variation and the sudden change of phase difference of the first two POD modes for the flow with $k=1$ initial perturbation: (a) from the projection of full simulation; (b) from the solution of the two-mode model. ——, phase difference between $a_{1,1}$ and $a_{1,2}$; — · —·, shear-layer thickness δ_g.

coefficients are approximately 180° out of phase, and after saturation, the coefficients are approximately in phase. Figure 8 reveals that the change in thickness (increasing or decreasing) is related to the phase difference between the two modes. Though the physical mechanism for this is not clear, it is clear that a phase change of about 180° occurs when thickness stops growing rapidly (i.e. when saturation occurs). A similar change in phase happens also at the second peak in thickness. This phenomenon has been successfully captured by the two-mode model as well. Note that the discussion about the phase difference is meaningful only when the amplitudes of the relevant modes are big enough. For this reason, to avoid any confusion, the plot is intentionally masked where the amplitude is too low.

This dependence on phase relationship between the two POD modes is reminiscent of the study of Monkewitz (1988), which looked at the phase relationship between the fundamental and subharmonic, and its effect on pairing. In our case, however, the phase relationship is between two POD modes of the same spatial frequency. Note that energy production rates in Galerkin models were studied by Noack *et al.* (2005), and similar techniques could be used to predict the envelope of growth and decay shown in figure 7.

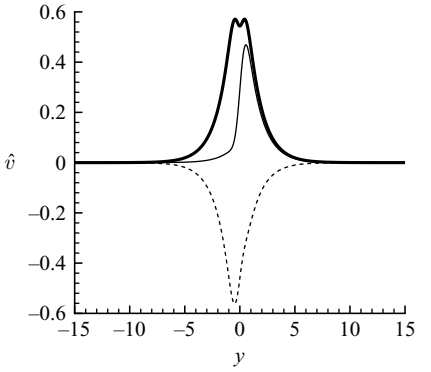

FIGURE 9. $\hat{v}$ of the most unstable eigenfunction for $k = 2$. The thin solid line represents the real value, the thin dashed line represents the imaginary value, and the thick solid line represents the absolute value.

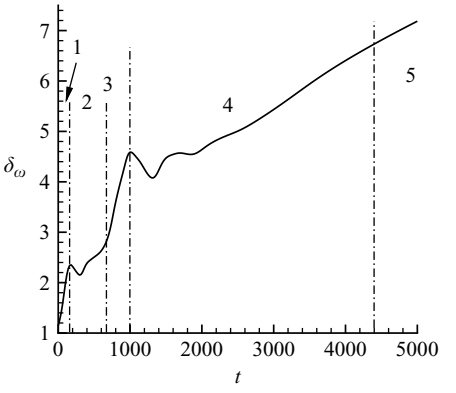

FIGURE 10. Vorticity thickness δ_ω for the flow with $k = 2$ initial perturbation: five developing stages are marked (see text for a description).

4.3. *Vortex pairing transient*

In this case, to study the vortex paring, which needs both $k = 1$ and $k = 2$ to describe it, we seeded initially the most unstable eigenfunction for $k = 2$ (figure 9) with small amplitude ($0.02\Delta U$) and allowed the unstable $k = 1$ to be generated naturally by numerical noise. As the shear thickness grows in time, the $k = 1$ mode eventually becomes more unstable than the $k = 2$ mode and grows rapidly to dominate the flow and trigger vortex pairing.

Figure 10 shows the evolution of the shear-layer thickness to illustrate this complex dynamics. Five stages in the development can be identified (see figure 1 for visual identification by vortex structures) as: 1, $k = 2$ vortices roll up; 2, $k = 2$ modes become stable at this thickness; 3, $k = 1$ modes are introduced (primarily owing to numerical noise), are more unstable, and cause vortex pairing; 4, $k = 1$ modes become stable; 5, perturbations have decayed, and viscous dissipation dominates.

With the same rescaling and empirical mode decomposition, table 2 shows the energy of the modes from this more complex dataset. This time, the first POD modes of $k = 1$ and $k = 2$ share the largest portion of the energy, and the energy contained in all other modes is small.

(k, n)	λ	energy (%)
(2, 1)	37.9	55.2
(1, 1)	27.5	40.1
(2, 2)	1.6	2.3
(1, 2)	0.9	1.3
All $k = 0$		0.6

TABLE 2. Energy contained in different modes for the flow with $k = 2$ initial perturbation.

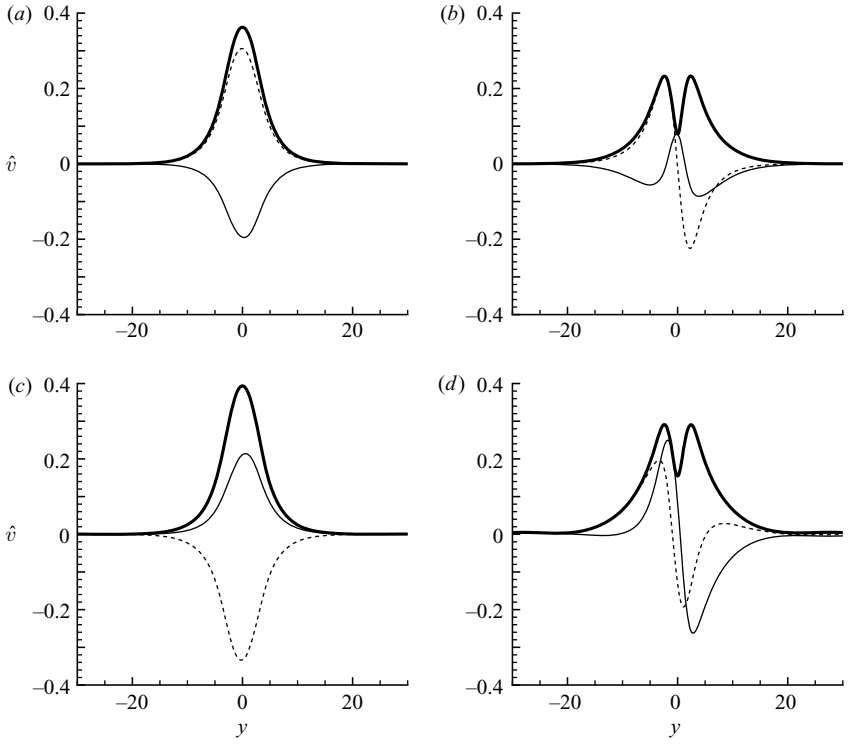

FIGURE 11. $\hat{v}$ for POD mode (*a*) $(k, n) = (1, 1)$, (*b*) $(k, n) = (1, 2)$, (*c*) $(k, n) = (2, 1)$, and (*d*) $(k, n) = (2, 2)$. The thin solid line represents the real value, the thin dashed line represents the imaginary value, and the thick solid line represents the absolute value.

Figure 11 shows the $\hat{v}$ components of the four most energetic modes, which together capture 98.9 % of the total energy.

The difference between $n = 1$ and $n = 2$ modes is similar for both $k = 1$ and $k = 2$. We can compare their shapes to the most unstable eigenfunction for both wavenumbers (figure 4 and 9), and then make the same argument as in § 4.2 to explain the importance of including $n = 2$ modes despite their small energy. In fact, using a two-mode model with only (2, 1) and (2, 2) modes, we can still capture vortex roll-up as in the single frequency case studied before, though mode (2, 2) is small in energy. (The two-mode model for the two-frequency case is not shown separately, as it is very close to the single-frequency case and we concentrate on the four-mode model in this section.) On the other hand, a two-mode model with the most energetic (2, 1) and (1, 1) modes is

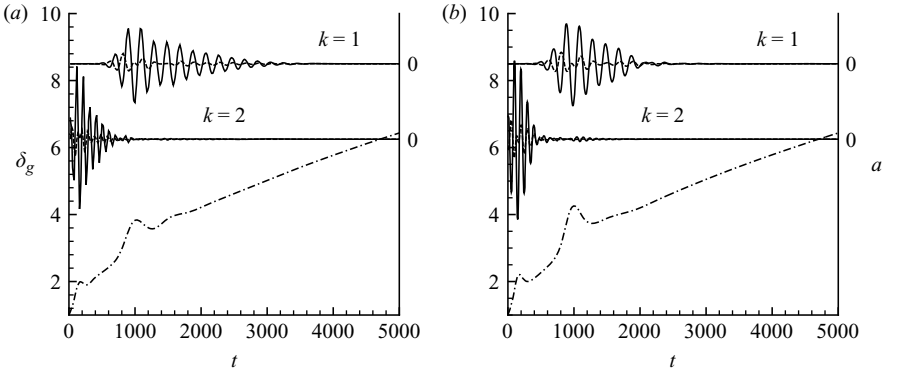

FIGURE 12. Comparison of the dynamic behaviour of the flow with $k = 2$ initial perturbation: (*a*) the projection of full simulation; (*b*) the solution of 4-mode model. ——, time coefficients $a_{1,1}(t)$ and $a_{2,1}(t)$; – – –, time coefficients $a_{1,2}(t)$ and $a_{2,2}(t)$; — · —, the shear-layer thickness δ_g. (*a*) and (*b*) have same scales for $a_{k,n}(t)$.

unstable, and cannot capture the dynamics successfully. This numerical experiment illustrates the need to retain the second POD modes with different shape.

It is not surprising that all four modes are required in order to describe both vortex roll-up and pairing processes in the two-frequency case. Figure 12(*a*) shows the time coefficients of modes $(k, n) = (1, 1)$, $(1, 2)$, $(2, 1)$ and $(2, 2)$, computed by projecting the data from the full simulation. The figure clearly illustrates the evolution of the coefficients corresponding to the five distinct stages of shear-layer development described above: first the $k = 2$ vortices grow, then saturate and gradually damp; then the energy is transferred to the $k = 1$ mode (pairing and merging), until this too is damped and only viscous diffusion remains.

Clearly, a two-mode model will not be enough to completely describe this more complex system with two characteristic wavenumbers. The dynamical model with all four modes $(k, n) = (1, 1)$, $(1, 2)$, $(2, 1)$ and $(2, 2)$ is constructed and gives results very close to the projection results as shown in figure 12(*b*). This four-mode model captures the dynamics already captured by the two-mode model with some improvement, and in addition also describes the vortex pairing process successfully.

As in the previous section, here for each wavenumber, we can also observe that the phase difference between the first two POD modes changes suddenly by about 180° when saturation begins (see figure 13). This behaviour has been successfully captured by the four-mode model as well. As in the single-wavenumber case, we masked portions of the plot where the amplitudes were small. Further investigation is required in order to understand better the physical mechanism behind this interesting phenomenon.

5. Conclusion

Using scaled POD and Galerkin projection, we can build a model based on a few basis functions to describe a temporally developing shear layer with its thickness growing in time. The basis functions are scaled (dynamically) in the y-direction so that in the scaled coordinates, the shear-layer thickness remains constant in time. The y-direction velocity v is scaled accordingly to satisfy the continuity equation, and an appropriate change is made to the definition of the inner product as well. In our study, we noticed the dynamic importance of the second POD mode (for both

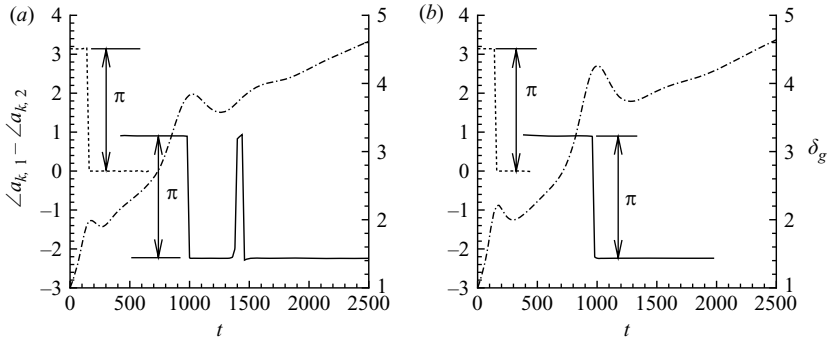

FIGURE 13. The relation between the shear-layer thickness variation and the sudden change of the phase difference of the first two POD modes for the flow with $k = 2$ initial perturbation: (*a*) from the projection of full simulation; (*b*) from the solution of the four-mode model. ——, phase difference between $a_{1,1}$ and $a_{1,2}$; – – –, phase difference between $a_{2,1}$ and $a_{2,2}$; — · —·, shear-layer thickness δ_g.

wavenumbers $k = 1$ and 2), though it captures much less energy than the first POD mode. We observe that the phase difference between the first and second POD mode plays a significant role in the shear layer spreading, and the growth in amplitude of the main energy-containing mode.

A two-mode model is constructed by projection of the incompressible Navier–Stokes equations onto the first and second POD modes with wavenumber $k = 1$. This model is simple and can describe the vortex roll-up, nonlinear saturation, and viscous damping. A more complex four-mode model can also be obtained by projection onto the first and second POD modes of wavenumbers $k = 1$ and 2. Applying this model to a shear flow, we see a more accurate description than the two-mode model, as we expect. More importantly, we see that the four-mode model successfully captures the vortex pairing/merging behaviour, as eventually the $k = 1$ mode becomes more unstable. In the future, we hope to use models such as these to the study the effects of external forcing (particularly high-frequency forcing), and ultimately to develop models suitable for feedback control, for instance to enhance or suppress spreading of the shear layer and growth of disturbances.

We thank Bernd Noack for many helpful suggestions, and the reviewers for especially constructive criticism. This work was supported by the AFOSR, grant FA9550-05-1-0369, and the NSF, grant CMS-0347239. M. W. would also like to acknowledge the support from Sandia-University Research Program (SURP) by Sandia National Laboratories.

Appendix A. Equations and the coefficients in the two-mode model

The differential equations for scaling variable g and coefficient vector $\boldsymbol{a} = (a_{1,1} \;\; a_{1,2})^T$ for the two-mode model of temporal shear-layer flow are given as

$$\dot{g} = \frac{c_{01}}{n_0} a_{1,1} a_{1,1}^* g + \frac{c_{02}}{n_0} a_{1,2} a_{1,2}^* g + \frac{c_{03}}{n_0} a_{1,1} a_{1,2}^* g + \frac{c_{04}}{n_0} a_{1,2} a_{1,1}^* g + \frac{1}{Re} \frac{d_0}{n_0} g^3, \tag{A 1}$$

and

$$\boldsymbol{A}\dot{\boldsymbol{a}} = \left(\boldsymbol{B} + \frac{1}{Re} \boldsymbol{D} + \frac{\dot{g}}{g} \boldsymbol{E} \right) \boldsymbol{a}, \tag{A 2}$$

where matrices $\boldsymbol{A}$, $\boldsymbol{B}$, $\boldsymbol{D}$, and $\boldsymbol{E}$ are defined by

$$\boldsymbol{A} = \begin{bmatrix} g^2 n_{11g} + n_{11} & g^2 n_{12g} + n_{12} \\ g^2 n_{21g} + n_{21} & g^2 n_{22g} + n_{22} \end{bmatrix}, \quad \boldsymbol{B} = \begin{bmatrix} g^2 c_{11g} + c_{11} & g^2 c_{12g} + c_{12} \\ g^2 c_{21g} + c_{21} & g^2 c_{22g} + c_{22} \end{bmatrix}, \qquad (\mathrm{A}\,3a, b)$$

$$\boldsymbol{D} = \begin{bmatrix} -(2\pi/L)^2(g^2 n_{11g} + n_{11}) + (g^2 d_{11g} + d_{11})g^2 \\ -(2\pi/L)^2(g^2 n_{12g} + n_{12}) + (g^2 d_{12g} + d_{12})g^2 \\ -(2\pi/L)^2(g^2 n_{21g} + n_{21}) + (g^2 d_{21g} + d_{21})g^2 \\ -(2\pi/L)^2(g^2 n_{22g} + n_{22}) + (g^2 d_{22g} + d_{22})g^2 \end{bmatrix}, \qquad (\mathrm{A}\,3c)$$

$$\boldsymbol{E} = \begin{bmatrix} g^2 e_{11g} + e_{11} & g^2 e_{12g} + e_{12} \\ g^2 e_{21g} + e_{21} & g^2 e_{22g} + e_{22} \end{bmatrix}, \qquad (\mathrm{A}\,3d)$$

with all coefficients defined below:

$$n_0 = \int \left(y \frac{\mathrm{d}u_0}{\mathrm{d}y} \right)^2 \mathrm{d}y, \qquad n_{11g} = \int \hat{u}_{1,1} \hat{u}_{1,1}^* \, \mathrm{d}y, \qquad n_{11} = \int \hat{v}_{1,1} \hat{v}_{1,1}^* \, \mathrm{d}y,$$

$$n_{12g} = \int \hat{u}_{1,2} \hat{u}_{1,1}^* \, \mathrm{d}y, \qquad n_{12} = \int \hat{v}_{1,2} \hat{v}_{1,1}^* \, \mathrm{d}y,$$

$$n_{21g} = \int \hat{u}_{1,1} \hat{u}_{1,2}^* \, \mathrm{d}y, \qquad n_{21} = \int \hat{v}_{1,1} \hat{v}_{1,2}^* \, \mathrm{d}y,$$

$$n_{22g} = \int \hat{u}_{1,2} \hat{u}_{1,2}^* \, \mathrm{d}y, \qquad n_{22} = \int \hat{v}_{1,2} \hat{v}_{1,2}^* \, \mathrm{d}y,$$

$$c_{01} = -\int \left(\hat{v}_{1,1} \frac{\mathrm{d}\hat{u}_{1,1}^*}{\mathrm{d}y} + \hat{v}_{1,1}^* \frac{\mathrm{d}\hat{u}_{1,1}}{\mathrm{d}y} \right) y \frac{\mathrm{d}u_0}{\mathrm{d}y} \mathrm{d}y, \quad c_{02} = -\int \left(\hat{v}_{1,2} \frac{\mathrm{d}\hat{u}_{1,2}^*}{\mathrm{d}y} + \hat{v}_{1,2}^* \frac{\mathrm{d}\hat{u}_{1,2}}{\mathrm{d}y} \right) y \frac{\mathrm{d}u_0}{\mathrm{d}y} \, \mathrm{d}y,$$

$$c_{03} = -\int \left(\hat{v}_{1,1} \frac{\mathrm{d}\hat{u}_{1,2}^*}{\mathrm{d}y} + \hat{v}_{1,2}^* \frac{\mathrm{d}\hat{u}_{1,1}}{\mathrm{d}y} \right) y \frac{\mathrm{d}u_0}{\mathrm{d}y} \mathrm{d}y, \quad c_{04} = -\int \left(\hat{v}_{1,2} \frac{\mathrm{d}\hat{u}_{1,1}^*}{\mathrm{d}y} + \hat{v}_{1,1}^* \frac{\mathrm{d}\hat{u}_{1,2}}{\mathrm{d}y} \right) y \frac{\mathrm{d}u_0}{\mathrm{d}y} \, \mathrm{d}y,$$

$$c_{11g} = -\int \left(\frac{2\pi}{L} \mathrm{i} u_0 \hat{u}_{1,1} + \hat{v}_{1,1} \frac{\mathrm{d}u_0}{\mathrm{d}y} \right) \hat{u}_{1,1}^* \, \mathrm{d}y, \qquad c_{11} = -\int \frac{2\pi}{L} \mathrm{i} u_0 \hat{v}_{1,1} \hat{v}_{1,1}^* \, \mathrm{d}y,$$

$$c_{12g} = -\int \left(\frac{2\pi}{L} \mathrm{i} u_0 \hat{u}_{1,2} + \hat{v}_{1,2} \frac{\mathrm{d}u_0}{\mathrm{d}y} \right) \hat{u}_{1,1}^* \, \mathrm{d}y, \qquad c_{12} = -\int \frac{2\pi}{L} \mathrm{i} u_0 \hat{v}_{1,2} \hat{v}_{1,1}^* \, \mathrm{d}y,$$

$$c_{21g} = -\int \left(\frac{2\pi}{L} \mathrm{i} u_0 \hat{u}_{1,1} + \hat{v}_{1,1} \frac{\mathrm{d}u_0}{\mathrm{d}y} \right) \hat{u}_{1,2}^* \, \mathrm{d}y, \qquad c_{21} = -\int \frac{2\pi}{L} \mathrm{i} u_0 \hat{v}_{1,1} \hat{v}_{1,2}^* \, \mathrm{d}y,$$

$$c_{22g} = -\int \left(\frac{2\pi}{L} \mathrm{i} u_0 \hat{u}_{1,2} + \hat{v}_{1,2} \frac{\mathrm{d}u_0}{\mathrm{d}y} \right) \hat{u}_{1,2}^* \, \mathrm{d}y, \qquad c_{22} = -\int \frac{2\pi}{L} \mathrm{i} u_0 \hat{v}_{1,2} \hat{v}_{1,2}^* \, \mathrm{d}y,$$

$$\mathrm{d}_0 = \int \frac{\mathrm{d}^2 u_0}{\mathrm{d}y^2} y \frac{\mathrm{d}u_0}{\mathrm{d}y} \, \mathrm{d}y, \quad \mathrm{d}_{11g} = \int \frac{\mathrm{d}^2 \hat{u}_{1,1}}{\mathrm{d}y^2} \hat{u}_{1,1}^* \, \mathrm{d}y, \quad \mathrm{d}_{11} = \int \frac{\mathrm{d}^2 \hat{v}_{1,1}}{\mathrm{d}y^2} \hat{v}_{1,1}^* \, \mathrm{d}y,$$

$$d_{12g} = \int \frac{\mathrm{d}^2 \hat{u}_{1,2}}{\mathrm{d}y^2} \hat{u}_{1,1}^* \, \mathrm{d}y, \qquad d_{12} = \int \frac{\mathrm{d}^2 \hat{v}_{1,2}}{\mathrm{d}y^2} \hat{v}_{1,1}^* \, \mathrm{d}y,$$

$$d_{21g} = \int \frac{\mathrm{d}^2\hat{u}_{1,1}}{\mathrm{d}y^2}\hat{u}^*_{1,2}\,\mathrm{d}y, \qquad d_{21} = \int \frac{\mathrm{d}^2\hat{v}_{1,1}}{\mathrm{d}y^2}\hat{v}^*_{1,2}\,\mathrm{d}y,$$

$$d_{22g} = \int \frac{\mathrm{d}^2\hat{u}_{1,2}}{\mathrm{d}y^2}\hat{u}^*_{1,2}\,\mathrm{d}y, \qquad d_{22} = \int \frac{\mathrm{d}^2\hat{v}_{1,2}}{\mathrm{d}y^2}\hat{v}^*_{1,2}\,\mathrm{d}y,$$

$$e_{11g} = -\int y\frac{\mathrm{d}\hat{u}_{1,1}}{\mathrm{d}y}\hat{u}^*_{1,1}\,\mathrm{d}y, \qquad e_{11} = -\int \left(y\frac{\mathrm{d}\hat{v}_{1,1}}{\mathrm{d}y} - \hat{v}_{1,1}\right)\hat{v}^*_{1,1}\,\mathrm{d}y,$$

$$e_{12g} = -\int y\frac{\mathrm{d}\hat{u}_{1,2}}{\mathrm{d}y}\hat{u}^*_{1,1}\,\mathrm{d}y, \qquad e_{12} = -\int \left(y\frac{\mathrm{d}\hat{v}_{1,2}}{\mathrm{d}y} - \hat{v}_{1,2}\right)\hat{v}^*_{1,1}\,\mathrm{d}y,$$

$$e_{21g} = -\int y\frac{\mathrm{d}\hat{u}_{1,1}}{\mathrm{d}y}\hat{u}^*_{1,2}\,\mathrm{d}y, \qquad e_{21} = -\int \left(y\frac{\mathrm{d}\hat{v}_{1,1}}{\mathrm{d}y} - \hat{v}_{1,1}\right)\hat{v}^*_{1,2}\,\mathrm{d}y,$$

$$e_{22g} = -\int y\frac{\mathrm{d}\hat{u}_{1,2}}{\mathrm{d}y}\hat{u}^*_{1,2}\,\mathrm{d}y, \qquad e_{22} = -\int \left(y\frac{\mathrm{d}\hat{v}_{1,2}}{\mathrm{d}y} - \hat{v}_{1,2}\right)\hat{v}^*_{1,2}\,\mathrm{d}y.$$

Appendix B. Equations in the four-mode model

The differential equations for scaling variable g and coefficient vector

$$\boldsymbol{a} = (a_{1,1}\ \ a_{1,2}\ \ a_{2,1}\ \ a_{2,2})^T$$

for the four-mode model are given as

$$\begin{aligned}\dot{g} = {} & \frac{c_{01}}{n_0}a_{1,1}a^*_{1,1}g + \frac{c_{02}}{n_0}a_{1,2}a^*_{1,2}g + \frac{c_{03}}{n_0}a_{1,1}a^*_{1,2}g + \frac{c_{04}}{n_0}a_{1,2}a^*_{1,1}g \\ & + \frac{c_{05}}{n_0}a_{2,1}a^*_{2,1}g + \frac{c_{06}}{n_0}a_{2,2}a^*_{2,2}g + \frac{c_{07}}{n_0}a_{2,1}a^*_{2,2}g + \frac{c_{08}}{n_0}a_{2,2}a^*_{2,1}g + \frac{1}{Re}\frac{d_0}{n_0}g^3, \end{aligned} \tag{B 1}$$

and

$$\boldsymbol{A}\dot{\boldsymbol{a}} = \left(\boldsymbol{B} + \frac{1}{Re}\boldsymbol{D} + \frac{\dot{g}}{g}\boldsymbol{E}\right)\boldsymbol{a} + \boldsymbol{N}, \tag{B 2}$$

where matrix $\boldsymbol{N}$ includes all terms nonlinear to $a_{k,n}$ as

$$\boldsymbol{N} = \begin{bmatrix} (g^2c_{13g} + c_{13})a^*_{1,1}a_{2,1} + (g^2c_{14g} + c_{14})a^*_{1,1}a_{2,2} + (g^2c_{15g} + c_{15})a^*_{1,2}a_{2,1} \\ \quad + (g^2c_{16g} + c_{16})a^*_{1,2}a_{2,2} \\ (g^2c_{23g} + c_{23})a^*_{1,1}a_{2,1} + (g^2c_{24g} + c_{24})a^*_{1,1}a_{2,2} + (g^2c_{25g} + c_{25})a^*_{1,2}a_{2,1} \\ \quad + (g^2c_{26g} + c_{26})a^*_{1,2}a_{2,2} \\ (g^2c_{33g} + c_{33})a_{1,1}a_{1,1} + (g^2c_{34g} + c_{34})a_{1,2}a_{1,2} + (g^2c_{35g} + c_{35})a_{1,1}a_{1,2} \\ (g^2c_{43g} + c_{43})a_{1,1}a_{1,1} + (g^2c_{44g} + c_{44})a_{1,2}a_{1,2} + (g^2c_{45g} + c_{45})a_{1,1}a_{1,2} \end{bmatrix}, \tag{B 3}$$

and other matrices for terms linear to $a_{k,n}$ have blocks of zeros as shown below:

$$\boldsymbol{A} = \begin{bmatrix} \boldsymbol{A}_1 & 0 \\ 0 & \boldsymbol{A}_2 \end{bmatrix},\ \boldsymbol{B} = \begin{bmatrix} \boldsymbol{B}_1 & 0 \\ 0 & \boldsymbol{B}_2 \end{bmatrix},\ \boldsymbol{D} = \begin{bmatrix} \boldsymbol{D}_1 & 0 \\ 0 & \boldsymbol{D}_2 \end{bmatrix},\ \boldsymbol{E} = \begin{bmatrix} \boldsymbol{E}_1 & 0 \\ 0 & \boldsymbol{E}_2 \end{bmatrix}, \tag{B 4}$$

with sub-matrices defined by

$$\boldsymbol{A}_1 = \begin{bmatrix} g^2 n_{11g} + n_{11} & g^2 n_{12g} + n_{12} \\ g^2 n_{21g} + n_{21} & g^2 n_{22g} + n_{22} \end{bmatrix}, \quad \boldsymbol{A}_2 = \begin{bmatrix} g^2 n_{31g} + n_{31} & g^2 n_{32g} + n_{32} \\ g^2 n_{41g} + n_{41} & g^2 n_{42g} + n_{42} \end{bmatrix},$$

$$\boldsymbol{B}_1 = \begin{bmatrix} g^2 c_{11g} + c_{11} & g^2 c_{12g} + c_{12} \\ g^2 c_{21g} + c_{21} & g^2 c_{22g} + c_{22} \end{bmatrix}, \quad \boldsymbol{B}_2 = \begin{bmatrix} g^2 c_{31g} + c_{31} & g^2 c_{32g} + c_{32} \\ g^2 c_{41g} + c_{41} & g^2 c_{42g} + c_{42} \end{bmatrix},$$

$$\boldsymbol{D}_1 = \begin{bmatrix} -(2\pi/L)^2(g^2 n_{11g} + n_{11}) + (g^2 d_{11g} + d_{11})g^2 \\ -(2\pi/L)^2(g^2 n_{12g} + n_{12}) + (g^2 d_{12g} + d_{12})g^2 \\ -(2\pi/L)^2(g^2 n_{21g} + n_{21}) + (g^2 d_{21g} + d_{21})g^2 \\ -(2\pi/L)^2(g^2 n_{22g} + n_{22}) + (g^2 d_{22g} + d_{22})g^2 \end{bmatrix},$$

$$\boldsymbol{D}_2 = \begin{bmatrix} -(2\pi/L)^2(g^2 n_{31g} + n_{31}) + (g^2 d_{31g} + d_{31})g^2 \\ -(2\pi/L)^2(g^2 n_{32g} + n_{32}) + (g^2 d_{32g} + d_{32})g^2 \\ -(2\pi/L)^2(g^2 n_{41g} + n_{41}) + (g^2 d_{41g} + d_{41})g^2 \\ -(2\pi/L)^2(g^2 n_{42g} + n_{42}) + (g^2 d_{42g} + d_{42})g^2 \end{bmatrix},$$

$$\boldsymbol{E}_1 = \begin{bmatrix} g^2 e_{11g} + e_{11} & g^2 e_{12g} + e_{12} \\ g^2 e_{21g} + e_{21} & g^2 e_{22g} + e_{22} \end{bmatrix}, \quad \boldsymbol{E}_2 = \begin{bmatrix} g^2 e_{31g} + e_{31} & g^2 e_{32g} + e_{32} \\ g^2 e_{41g} + e_{41} & g^2 e_{42g} + e_{42} \end{bmatrix}.$$

The equations for coefficients are too many to be listed here.

REFERENCES

Brown, G. L. & Roshko, A. 1974 On density effects and large structure in turbulent mixing layers. *J. Fluid Mech.* **64**, 775–816.

Chomaz, J.-M. 2005 Global instabilities in spatially developing flows: non-normality and nonlinearity. *Annu. Rev. Fluid Mech.* **37**, 357–339.

Drazin, P. G. & Reid, W. H. 2004 *Hydrodynamic Stability*, 2nd edn. Cambridge University Press.

Freund, J. B. 1997 Proposed inflow/outflow boundary condition for direct computation of aerodynamic sound. *AIAA J.* **35**, 740–742.

Guckenheimer, J. & Holmes, P. J. 1983 *Nonlinear Oscillations, Dynamical Systems, and Bifurcations of Vector Fields*, *Applied Mathematical Sciences*, vol. 42. Springer.

Ho, C. M. & Huerre, P. 1984 Perturbed free shear layers. *Annu. Rev. Fluid Mech.* **16**, 365–424.

Holmes, P., Lumley, J. L. & Berkooz, G. 1996 *Turbulence, Coherent Structures, Dynamical Systems and Symmetry*. Cambridge University Press.

Monkewitz, P. A. 1988 Subharmonic resonance, pairing and shredding in the mixing layer. *J. Fluid Mech.* **188**, 223–252.

Noack, B. R. & Eckelmann, H. 1994 A global stability analysis of the steady and periodic cylinder wake. *J. Fluid Mech.* **270**, 297–330.

Noack, B. R., Afanasiev, K., Morzyński, M., Tadmor, G. & Thiele, F. 2003 A hierarchy of low-dimensional models for the transient and post-transient cylinder wake. *J. Fluid Mech.* **497**, 335–363.

Noack, B. R., Pelivan, I., Tadmor, G., Morzyński, M. & Comte, P. 2004 Robust low-dimensional Galerkin models of natural and actuated flows. In *Fourth Aeroacoustics Workshop*. *RWTH Aachen 26–27 February 2004*.

Noack, B. R., Papas, P. & Monkewitz, P. A. 2005 The need for a pressure-term representation in empirical Galerkin models of incompressible shear flow. *J. Fluid Mech.* **523**, 339–365.

Rayleigh, Lord 1880 On the stability, or instability, of certain fluid motions. *Proc. Lond. Math. Soc.* **11**, 57–70.

Rowley, C. W. & Marsden, J. E. 2000 Reconstruction equations and the Karhunen–Loève expansion for systems with symmetry. *Physica* D **142**, 1–19.

Rowley, C. W. & Williams, D. R. 2006 Dynamics and control of high-Reynolds-number flow over open cavities. *Annu. Rev. Fluid Mech.* **38**, 251–276.

Rowley, C. W., Kevrekidis, I. G., Marsden, J. E. & Lust, K. 2003 Reduction and reconstruction for self-similar dynamical systems. *Nonlinearity* **16**, 1257–1275.

Saffman, P. G. & Baker, G. R. 1979 Vortex interactions. *Annu. Rev. Fluid Mech.* **11**, 95–122.

Schlichting, H. & Gersten, K. 2000 *Boundary-Layer Theory*, 8th edn. Springer.

Schmid, P. J. & Henningson, D. S. 2001 *Stability and Transition in Shear Flows*, *Applied Mathematical Sciences*, vol. 142. Springer.

Stanek, M. J., Raman, G., Kibens, V., Ross, J. A., Odedra, J. & Peto, J. W. 2001 Suppression of cavity resonance using high frequency forcing – the characteristic signature of effective devices. *AIAA Paper* 2001-2128.

Tam, C. K. W. & Block, P. J. W. 1978 On the tones and pressure oscillations induced by flow over rectangular cavities. *J. Fluid Mech.* **89**, 373–399.

Tam, C. K. W. & Webb, J. C. 1993 Dispersion-relation-preserving finite difference schemes for computational acoustics. *J. Comput. Phys.* **107** (2), 262–281.

Thomsen, J. J. 2002 Some general effects of strong high-frequency excitation: stiffening, biasing, and smoothening. *J. Sound Vib.* **253**, 807–831.

Wei, M. & Freund, J. B. 2006 A noise-controlled free shear flow. *J. Fluid Mech.* **546**, 123–152.